ADVANCED MATERIALS
www.advmat.de

Engineering the Electronic Structure of Single-Atom Iron Sites with Boosted Oxygen Bifunctional Activity for Zinc–Air Batteries

Zhijun Li, Siqi Ji, Chang Xu, Leipeng Leng, Hongxue Liu, J. Hugh Horton, Lei Du, Jincheng Gao, Cheng He,* Xiaoying Qi, Qian Xu, and Junfa Zhu*

Rechargeable zinc–air batteries typically require efficient, durable, and inexpensive bifunctional electrocatalysts to support oxygen reduction/evolution reactions (ORR/OER). However, sluggish kinetics and mass transportation challenges must be addressed if the performance of these catalysts is to be enhanced. Herein, a strategy to fabricate a catalyst comprising atomically dispersed iron atoms supported on a mesoporous nitrogen-doped carbon support (Fe SAs/NC) with accessible metal sites and optimized electronic metal–support interactions is developed. Both the experimental results and theoretical calculations reveal that the engineered electronic structures of the metal active sites can regulate the charge distribution of Fe centers to optimize the adsorption/desorption of oxygenated intermediates. The Fe SAs/NC containing $Fe_1N_4O_1$ sites achieves remarkable ORR activity over the entire pH range, with half-wave potentials of 0.93, 0.83, and 0.75 V (vs reversible hydrogen electrode) in alkaline, acidic, and neutral electrolytes, respectively. In addition, it demonstrates a promising low overpotential of 320 mV at 10 mA cm^{-2} for OER in alkaline conditions. The zinc–air battery assembled with Fe SAs/NC exhibits superior performance than that of Pt/C+RuO_2 counterpart in terms of peak power density, specific capacity, and cycling stability. These findings demonstrate the importance of the electronic structure engineering of metal sites in directing catalytic activity.

1. Introduction

The development of advanced energy conversion and storage technologies is important to fulfill the purpose of clean energy usage and energy crisis alleviation.[1–3] For renewable energy systems, rechargeable metal–air batteries and proton-exchange-membrane fuel cells (PEMFCs) have attracted huge attention by virtue of high energy density, low cost, and environmental friendliness.[4–7] The efficiency of electrocatalysts employed in both energy systems is heavily dependent on electrochemical reactions associated with oxygen, including both the oxygen reduction reaction (ORR) and the oxygen evolution reaction (OER).[8–10] However, the poor activity and sluggish kinetics of four proton-coupled electron-transfer steps in ORR and OER severely hinder their application in zinc–air batteries.[11–13] Although precious-metal catalysts have been considered to be the benchmarks for use in zinc–air batteries (Pt for ORR side; RuO_2 and IrO_2 for OER side), their extremely high cost, natural scarcity, limited stability, and potential for competing methanol crossover and CO poisoning reactions have greatly limited their large-scale commercial implementation.[14,15] Therefore, development of efficient bifunctional electrocatalysts to overcome the sluggish kinetics of ORR in the discharging process and OER in the charging process is crucial for zinc–air batteries.[3,6,16]

Z. Li, S. Ji, L. Leng, H. Liu, J. H. Horton, J. Gao
Joint International Research Laboratory of Advanced Chemical Catalytic Materials & Surface Science
College of Chemistry and Chemical Engineering
Northeast Petroleum University
Daqing 163318, P. R. China
E-mail: zhijun.li@queensu.ca

C. Xu, C. He
State Key Laboratory for Mechanical Behavior of Materials
School of Materials Science and Engineering
Xi'an Jiaotong University
Xi'an 710049, P. R. China
E-mail: hecheng@mail.xjtu.edu.cn

The ORCID identification number(s) for the author(s) of this article can be found under https://doi.org/10.1002/adma.202209644.

DOI: 10.1002/adma.202209644

J. H. Horton
Department of Chemistry
Queen's University
Kingston, ON K7L 3N6, Canada

L. Du
Huangpu Hydrogen Energy Innovation Centre
School of Chemistry and Chemical Engineering
Guangzhou University
Guangzhou 510006, P. R. China

X. Qi
CAS Key Laboratory of Standardization and Measurement for Nanotechnology
National Center for Nanoscience and Technology
Beijing 100190, P. R. China

Q. Xu, J. Zhu
National Synchrotron Radiation Laboratory
University of Science and Technology of China
Hefei 230029, P. R. China

Single-atom catalysts (SACs), by virtue of their well-defined atomic structure, maximal metal utilization, unique electronic/geometric properties, and excellent activity and selectivity, have attracted considerable research attention.[17–26] Nitrogen-doped carbon (NC) supported transition metal-based SACs, which exhibit the merits of good electrical conductivity, low cost, environmental friendliness, and comparable catalytic activity with precious-metal counterparts, have been regarded as one of the potentially feasible alternatives to precious-metal-based electrocatalysts in ORR and OER.[27–30] For example, Chen et al. reported a polymerization–pyrolysis–evaporation strategy to synthesize N-doped porous carbon with atomically dispersed Fe_1-N_4 sites.[31] Experimental results and theoretical calculations demonstrated superior trifunctional electrocatalytic performance. Sun et al. described a single-atom Fe electrocatalyst by incorporating Fe-Phen complexes into the nanocages during the growth of ZIF-8, followed by pyrolysis under an inert atmosphere.[32] As a cathode catalyst for zinc–air batteries, it delivered remarkable electrochemical performances in alkaline conditions. Zhang and co-workers developed a clicking confinement strategy to create a single-atom cobalt electrocatalyst using cobalt-coordinated porphyrin and carbon nanotubes.[33] It exhibited impressive bifunctional oxygen electrocatalytic performance with an activity ΔE of merely 0.79 V. Nevertheless, further improvement in oxygen bifunctional electrocatalytic activity is still required to meet the real-life demands in energy storage systems.[20,34,35] In general, increasing the metal loading with a high number of exposed metal sites and optimizing the corresponding electronic structure are two important tactics to improve the intrinsic activity of electrocatalysts.[36–39] One grand challenge faced by NC-supported SACs is that when a high number of metal precursors are used but without a proper modification to the synthetic methods, these atomically dispersed metal sites tend to aggregate into large nanoclusters during pyrolysis, which is detrimental to electrocatalytic activity.[19,20] Another challenge is ensuring the maximal exposure of metal sites in a 3D NC matrix, with negligible numbers of metal sites being buried inside and inaccessible, to significantly minimize the mass transport effects.[28,37,40,41] Furthermore, engineering the electronic structure of metal sites by tuning coordination environments can further optimize the adsorption/desorption of oxygen intermediates to effectively enhance the kinetics and activity of SACs.[20,34,42] Therefore, creating an efficient approach to simultaneously expose high-density active sites and precisely tune the electronic structure in SACs is required to endow excellent bifunctional ORR and OER performance in rechargeable zinc–air batteries. Meeting these design requirements is the main goal of this paper.

In this work, we report on a straightforward strategy to create oxygen-modified isolated Fe sites distributed over a nitrogen-doped carbon catalyst (Fe SAs/NC), with one O atom coordinating with a single Fe atom and perpendicular to the Fe_1-N_4 plane. By regulating the electronic structure of the Fe sites through oxygen coordination at the optimized $Fe_1N_4O_1$ moieties, the highly exposed Fe sites in Fe SAs/NC displayed excellent bifunctional oxygen electrocatalytic activity, superior to that exhibited by commercial Pt/C and RuO_2 catalysts under alkaline conditions. In addition, it achieved excellent ORR activity in pH-universal electrolyte systems. Most importantly, the engineered electronic structure of optimized $Fe_1N_4O_1$ moieties demonstrated high performance in rechargeable zinc–air batteries and proton exchange membrane fuel cells (PEMFCs), highlighting the potential for energy conversion systems.

2. Results and Discussion

A combined polymer coating, wet chemistry adsorption, ammonia treatment, and pyrolysis approach was conducted to create a single-atom Fe catalyst over a mesoporous nitrogen-doped carbon catalyst (Fe SAs/NC). The detailed synthetic procedure is shown in **Figure 1**a. Zeolitic imidazolate framework-8 (ZIF-8) was coated with a mixture of dopamine and F127 in a mixed ethanol/H_2O solvent before addition of iron acetylacetonate solution (Figure S1, Supporting Information). The pH of the mixture was adjusted by ammonia solution to 8.5. After continuous stirring, the precipitates were collected and annealed under an argon atmosphere to obtain Fe SAs/NC (metal loading of 1.29 wt.%, Table S1, Supporting Information). The morphology of as-prepared Fe SAs/NC was illustrated by scanning electron microscopy (SEM) and transmission electron microscopy (TEM) observations (Figure 1b–d). After high-temperature carbonization, a concave morphology with sharp edges and interior cavities was noticed for Fe SAs/NC. This is associated with the anisotropic thermal shrinkage of ZIF-8 induced by a polymer coating.[43] A high-resolution TEM (HR-TEM) image and the corresponding ring-like selected-area electron diffraction (SAED) pattern of Fe SAs/NC confirms the absence of Fe nanoclusters in the catalyst (Figure 1e). A spherical-aberration-corrected high-angle annular dark-field scanning transmission electron microscopy (AC HAADF-STEM) imaging with sub-angstrom resolution demonstrated densely populated bright dots, marked with yellow circles, corresponding to heavier Fe atoms with different Z-contrast relative to the NC support (Figure 1f; Figure S2, Supporting Information). Energy-dispersive X-ray spectroscopy (EDS) elemental mapping unveils that the Fe, C, and N elements are uniformly distributed in Fe SAs/NC (Figure 1g). The reference sample of Fe_1/NC with atomic dispersion (metal loading of 0.91 wt.%) was prepared without the use of dopamine and F127 during the synthesis (Figures S3–S6 and Table S1, Supporting Information). The high-resolution Fe 2p spectrum demonstrates that no signal of metallic Fe was found in Fe_1/NC (Figure S7, Supporting Information). Moreover, the Fe $2p_{3/2}$ peak of Fe_1/NC was located at 710.9 eV, which is situated between Fe^0 and Fe^{2+}, suggesting the Fe species were positively charged ($Fe^{\delta+}$, $0 < \delta < 2$).[44–46] The high-resolution N 1s and C 1s spectra of Fe_1/NC were shown in Figures S8 and S9 and Table S2 (Supporting Information). The position of pyridinic-N of Fe_1/NC in Figure S8 (Supporting Information) was up-shifted 0.13 eV compared to that of NC (ZIF-8), implying the formation of Fe-pyridinic N sites. Two other reference samples were synthesized, the first undergoing the same synthesis process but without addition of Fe ions (denoted NC, Figures S10 and S11, and Table S1, Supporting Information) while the second, denoted NC (ZIF-8) was obtained by simple pyrolysis of ZIF-8 (Figures S12 and S13, Supporting Information). Raman spectrum of Fe SAs/NC showed a higher degree of structural

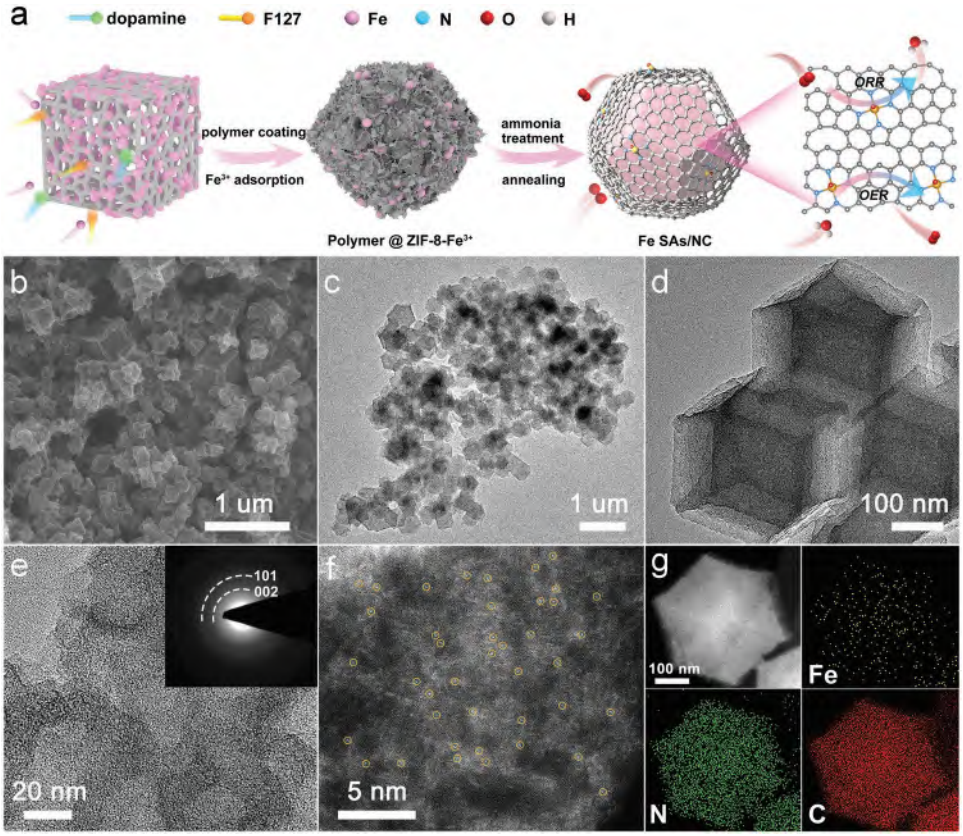

Figure 1. Synthesis and morphology characterization of Fe SAs/NC. a) Schematic illustration of the synthetic route. b) SEM image. c,d) TEM images, e) HR-TEM image, and SAED pattern (inset in (e)). f) High-resolution AC HAADF-STEM image. g) EDS elemental mappings.

defects, as indicated by a relatively higher I_D/I_G ratio of 1.45 compared to other references (Figure S14, Supporting Information). The mesoporous structure of Fe SAs/NC was confirmed by N_2 adsorption/desorption characterization (Figure S15 and Table S3, Supporting Information), where typical micro-/mesopores were observed. The combined use of dopamine, F127, and ammonia during the synthesis makes Fe SAs/NC possesses the highest porosity and specific surface area. This is favorable to the accessibility of metal active sites and reactant/electron transfer during the electrochemical reactions.[35,41]

The amorphous nature of the samples was confirmed by powder X-ray diffraction (XRD) shown in **Figure 2**a. The absence of bulk Fe in Fe SAs/NC reveals the high dispersion of Fe species, without larger aggregates, over the NC support. The chemical composition and electronic structure of Fe SAs/NC were investigated by X-ray photoelectron spectroscopy (XPS). The survey scan showed that the C, N, O, and Fe peaks are observed in Fe SAs/NC (Figure S16, Supporting Information). The high-resolution C 1s spectrum of Fe SAs/NC (Figure S17, Supporting Information) can be deconvolved into three peaks, corresponding to C—C/C=C at 284.6 eV, C=C—N at 285.8 eV, and O—C=O at 288.9 eV. The high-resolution Fe 2p spectrum (Figure 2b) was resolved into doublet peaks for Fe^{2+} (710.9 and 723.5 eV) and Fe^{3+} (715.5 and 728.3 eV), implying electron-deficient characteristics of the cationic Fe species.[44–46] The high-resolution N 1s spectrum in NC (Figure 2c; Table S4, Supporting Information) reveals the presence of three types of nitrogen species, being pyridinic-N at 398.2 eV, pyrrolic-N at 399.1 eV, and graphitic-N at 401.1 eV. After deposition of Fe single atoms over the NC support, the pyridinic-N peak was up-shifted 0.12 eV, suggesting the formation of Fe-pyridinic N sites. Fourier-transform infrared (FT-IR) spectra of samples are displayed in Figure S18 (Supporting Information). All of the data provides the typical feature of NC materials. The electron paramagnetic resonance (EPR) spectrum of Fe SAs/NC with a g value of 2.10 is shown in Figure S19 (Supporting Information), which is associated with the coordinatively unsaturated nature of Fe sites.

Synchrotron X-ray absorption near-edge structure (XANES) and extended X-ray absorption fine structure (EXAFS) spectroscopy were performed to investigate atomic dispersion, chemical state, and coordination environment of Fe species in Fe SAs/NC. Figure 2d shows that the adsorption edge of Fe SAs/NC is situated between those of FeO and Fe_2O_3 and more positive than that of FePc. This suggests these Fe species in Fe SAs/NC carry positive charges with the valance state between +2 and +3. Fourier-transformed k^2-weighted EXAFS spectra of the samples are shown in Figure 2e. These allow a more intuitive visualization of the local coordination structure. Fe SAs/NC delivered one dominant peak at 1.78 Å which is associated with Fe—N first shell coordination. Notably, this peak position is close to that of reference FePc. Moreover, no peaks from Fe—O and Fe—O—Fe coordination were observed in Fe

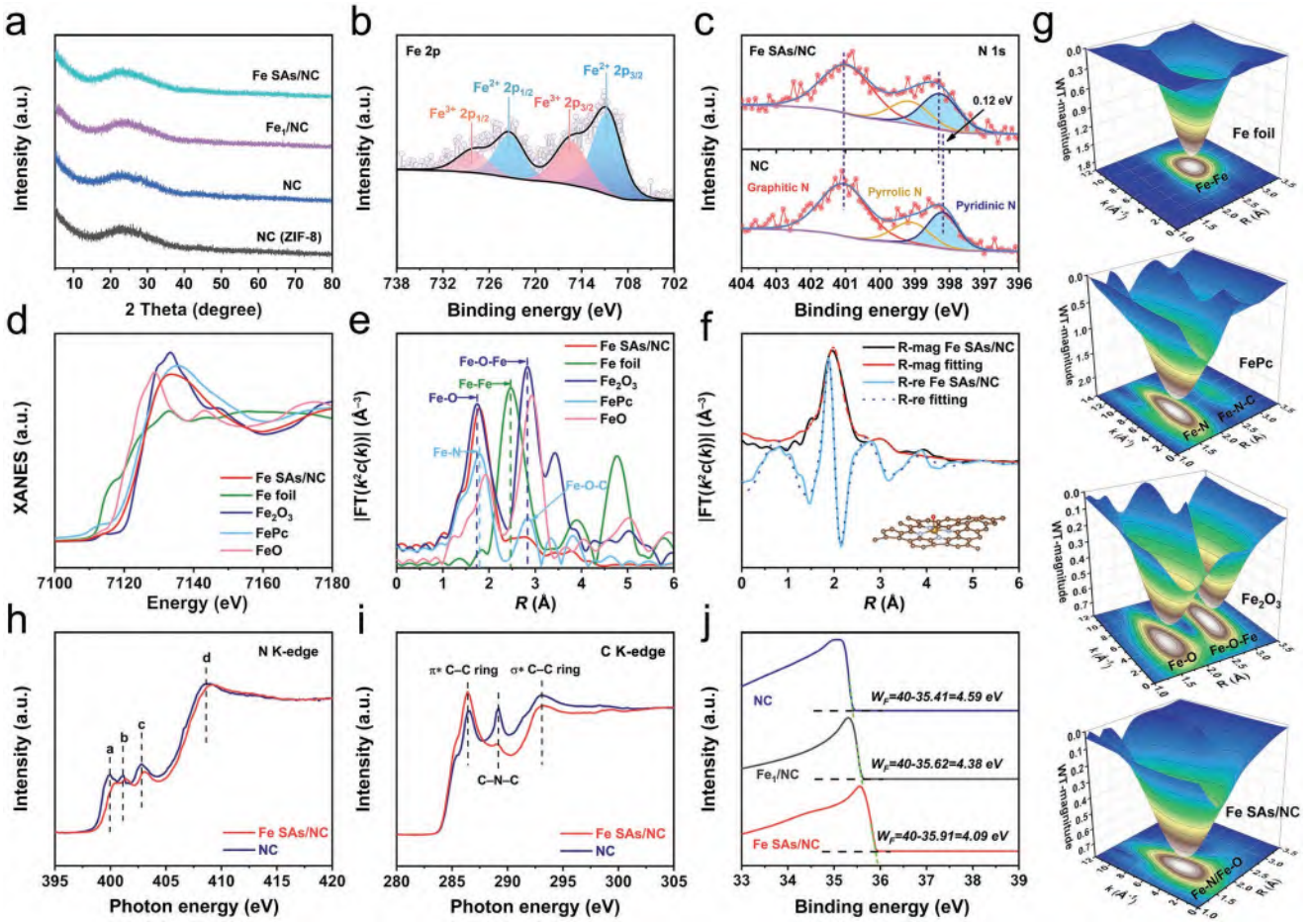

Figure 2. Atomic structural analysis of Fe SAs/NC. a) XRD patterns. b,c) High-resolution XPS Fe 2p (b) and N 1s (c) spectra. d) Fe K-edge XANES spectra. e) FT k^2-weighted Fe K-edge EXAFS spectra. f) EXAFS fitting results in R space (inset, schematic model of $Fe_1N_4O_1$). g) 3D contour WT-EXAFS plots. h,i) N (h) and C (i) K-edge XANES spectra. j) Secondary-electron tail threshold spectra.

SAs/NC, implying the vast majority of Fe species in the catalyst are atomically dispersed. Quantitative least-squares EXAFS fitting analysis (Figures 2f; Figure S20 and Table S5, Supporting Information) reveals that the Fe center is in a penta-coordinated geometry with four N atoms and one O atom to form an O_1–Fe_1–N_4 structure in Fe SAs/NC, with average Fe—N and Fe—O bond lengths of 1.99 Å and 2.04 Å, respectively. EXAFS wavelet transform (WT) analysis further confirmed the presence of the Fe—N/Fe—O path in Fe SAs/NC (Figure 2g). Overall, these results validate that the Fe species exist as isolated atoms in Fe SAs/NC. We further investigated the atomic dispersion and coordination environment of Fe species in Fe_1/NC reference sample, and the results demonstrate that these isolated Fe atoms are positively charged with Fe_1-N_4 coordination environment (Figure S21 and Table S5, Supporting Information).

Soft X-ray absorption spectroscopy (XAS) was then conducted to study the electronic properties of N and C in Fe SAs/NC and NC. Four dominant peaks are observed in the N K-edge spectra (Figure 2h) and they are associated with: a) π^* pyridinic N, b) π^* pyrrolic N, c) π^* graphitic N, and d) σ^* C—N bonding, respectively. Compared with NC, all of these peaks shifted to higher photon energies in Fe SAs/NC, meaning a substantial amount of electron density was transferred between C and N after deposition of Fe species. Moreover, the intensity of peak a is reduced when compared with that of NC, suggesting the formation of Fe–pyridinic N sites. The C K-edge spectra of Fe SAs/NC and NC (Figure 2i) exhibited characteristic peaks of the π^* C—C (286.8 eV), C—N—C (289.5 eV), and σ^* C—C (293.8 eV) peaks. In Fe SAs/NC, the intensity of the C—N—C peak was decreased, whereas the π^* C—C ring peak was increased. This can be explained by the electronic density change in the NC material after anchoring atomically dispersed Fe atoms. When compared with NC, the valence bands of Fe SAs/NC and Fe_1/NC shifted away from the Fermi level (Figure S22, Supporting Information), which is associated with a weakened binding with molecular oxygen. In addition, the valence band of Fe SAs/NC was intermediate to those of NC and Fe_1/NC. This suggests that the binding strength between the catalyst and molecular oxygen is neither too strong nor too weak. The work functions of Fe SAs/NC, Fe_1/NC, and NC were measured to be 4.09, 4.38, and 4.59 eV, respectively (Figure 2j). The smaller work function of Fe SAs/NC is highly desirable for obtaining high ORR activity.[47,48]

The ORR performance of these catalysts was examined using rotating disk electrode (RDE) and rotating ring-disk electrode (RRDE) measurements in 0.1 M KOH. The linear sweep

voltammetry (LSV) curves showed that the optimized catalyst loading of Fe SAs/NC was 0.23 mg cm^{-2} (Figure S23, Supporting Information). As shown in **Figure 3**a, Fe SAs/NC demonstrated an exceptional ORR activity with an early-onset potential (E_{onset}, defined as the potential at 0.1 mA cm^{-2}) of 1.11 V vs reversible hydrogen electrode (RHE, all potentials are referenced to RHE) and a half-wave potential ($E_{1/2}$) of 0.93 V, outperforming the benchmark Pt/C (E_{onset} of 1.00 V, $E_{1/2}$ of 0.85 V) and other references. Moreover, the ORR activity of Fe SAs/NC is among the best-performing non-precious-metal catalysts under alkaline conditions (Table S6, Supporting Information). The fast ORR kinetics (Figure 3b) of Fe SAs/NC was demonstrated by a smaller Tafel slope of 77.5 mV dec^{-1} compared to 108.8 mV dec^{-1} for Fe_1/NC, 119.1 mV dec^{-1} for NC, 127.7 mV dec^{-1} for Pt/C, and 169.3 mV dec^{-1} for NC (ZIF-8). As shown in Figure 3c, Fe SAs/NC presents the highest kinetic current densities (J_k) of 63.69 mA cm^{-2} and 25.84 mA cm^{-2} at 0.80 V and 0.85 V, respectively, significantly higher than those of Fe_1/NC (4.59 mA cm^{-2} and 2.51 mA cm^{-2}), Pt/C (15.75 mA cm^{-2} and 4.25 mA cm^{-2}), NC (6.67 mA cm^{-2} and 2.67 mA cm^{-2}), and ZIF-8 derived NC (0.78 mA cm^{-2} and 0.39 mA cm^{-2}). This further verified the excellent ORR activity of Fe SAs/NC. The electrochemical active surface area (ECSA) of these catalysts was calculated based on the positive relationship between ECSA and electrochemical double-layer capacitance (C_{dl}). As shown in Figure S24 (Supporting Information), the calculated C_{dl} of Fe SAs/NC is 8.07 mF cm^{-2}, which is larger than those of 2.93 mF cm^{-2} for Fe_1/NC, 7.36 mF cm^{-2} for Pt/C, 1.65 mF cm^{-2} for NC, and 0.77 mF cm^{-2} for NC (ZIF-8). The high C_{dl} value of Fe SAs/NC is beneficial to the fast kinetics and high utilization of active

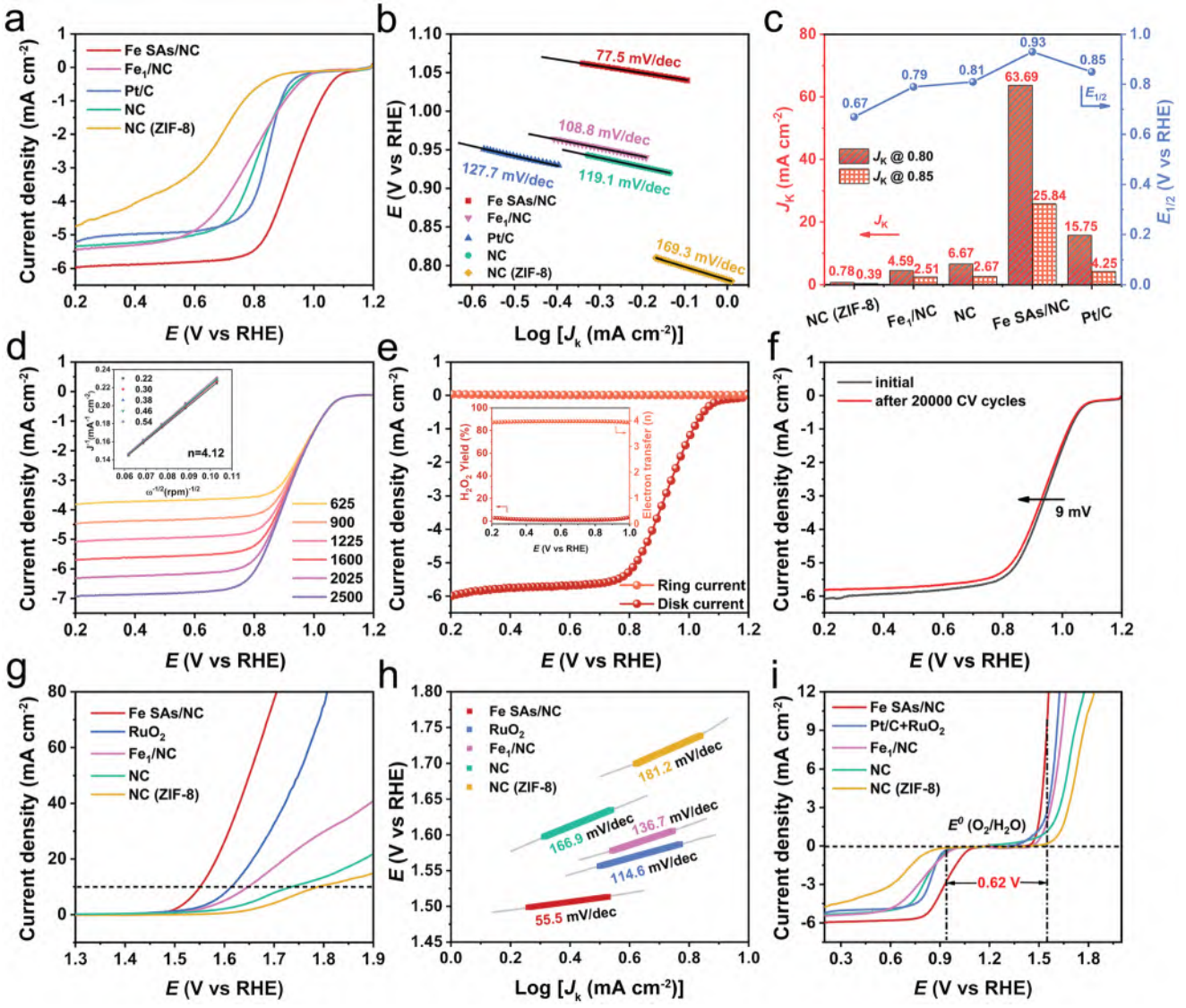

Figure 3. ORR and OER activity of Fe SAs/NC in 0.1 M KOH solution. a) ORR polarization curves and b) the corresponding Tafel plots. c) Comparisons of J_k at 0.80 V and 0.85 V of samples. d) ORR polarization curves of Fe SAs/NC at different rotating speeds (inset: K–L plots and electron-transfer numbers). e) RRDE measurements (inset: electron transfer number (n) and H_2O_2 selectivity). f) ORR polarization curves of Fe SAs/NC before and after 20 000 potential cycles. g) OER polarization curves and h) the corresponding Tafel plots. i) Overall polarization curves of samples within the ORR and OER potential window.

sites. Next, the ORR pathways of these catalysts were demonstrated by the Koutecký–Levich (K–L) plots derived from the LSV curves. The electron-transfer number (n) of Fe SAs/NC was determined to be 4.12 (Figure 3d), closer to the theoretical value of 4 than those of the references (Figures S25–S28, Supporting Information), suggesting the high 4-electron selectivity during the ORR pathway. This was supported by the RRDE measurements: the generated H_2O_2 yield is below 3% over the potential range from 0.2 V to 1.0 V, significantly lower than these references (Figures 3e; Figure S29, Supporting Information). To evaluate the critical role of these isolated Fe sites on ORR activity, KSCN poisoning experiments were performed. The resulting Fe SAs/NC (Figure S30, Supporting Information) exhibited ≈34 mV loss in $E_{1/2}$ after adding the KSCN solution, further verifying the important role of these Fe sites in ORR. In the case of Pt/C, ≈110 mV loss in $E_{1/2}$ was found (Figure S31, Supporting Information). The electrocatalytic stability of Fe SAs/NC was evaluated which manifests outstanding long-term stability with negligible activity decay in $E_{1/2}$ (≈9 mV) after 20 000 continuous potential cycles by accelerated durability tests. In addition, there were no observable morphological and structural changes for the catalyst after the durability test, validating its excellent stability (Figure S32, Supporting Information). In sharp contrast, serious activity decay of ≈40 mV was noticed for Pt/C (Figure S33, Supporting Information). Furthermore, chronoamperometric measurements were performed (Figure S34, Supporting Information) and the results show that the current density of Fe SAs/NC retained ≈90% after 550 min, superior to that of the commercial Pt/C catalyst (≈82% retained).

The electrochemical OER activities of catalysts were further measured in 0.1 M KOH solution. As shown in Figure 3g, Fe SAs/NC exhibited a smaller overpotential (η) of 320 mV when the current density reaches 10 mA cm^{-2}, revealing its superior OER activity compared with Fe_1/NC (422 mV), NC (510 mV), NC derived from ZIF-8 (560 mV), and RuO_2 (384 mV). The Tafel slope of Fe SAs/NC was determined to be 55.5 mV dec^{-1}, significantly smaller than these reference catalysts (Figure 3h), implying the fast OER kinetics. Of particular note is that both the η and Tafel slope of Fe SAs/NC are among the smallest values of reported OER electrocatalysts (Table S7, Supporting Information). Turnover frequency (TOF) values of these catalysts were calculated and the results show that 0.32 s^{-1} is obtained for Fe SAs/NC at the overpotential of 300 mV (Figure S35, Supporting Information), which is much higher than those of Fe_1/NC (0.09 s^{-1}) and RuO_2 (0.005 s^{-1}), revealing its high intrinsic activity. Fe SAs/NC also demonstrates robust OER stability with merely 9 mV activity decay after 3000 repeated cycles (Figure S36), Supporting Information. The performance stability of catalysts is essential to their practical applications.[16] Chronoamperometric and chronopotentiometric measurements were performed and strong evidence for the high OER stability of Fe SAs/NC was confirmed (Figures S37 and S38, Supporting Information). The ORR and OER bifunctional catalytic activity were further evaluated by the voltage gap (ΔE) between the $E_{j=10}$ for OER and the $E_{1/2}$ for ORR. Generally, a smaller value of ΔE reveals a better bifunctional electrocatalytic activity for a catalyst. As shown in Figure 3i, the ΔE of Fe SAs/NC was determined to be 0.62 V, much smaller than those of Fe_1/NC (0.86 V), NC (0.93 V), NC derived from ZIF-8 (1.12 V), Pt/C+RuO_2 (0.76 V), and most of the non-precious-metal bifunctional catalysts reported in the literature (Table S8, Supporting Information). These results strongly validate the excellent bifunctional electrocatalytic activity of Fe SAs/NC.

To validate the potential application of bifunctional Fe SAs/NC catalyst in energy conversion devices, a primary zinc–air battery was assembled with Fe SAs/NC loaded on nickel foam as an air cathode, a zinc plate as an anode, and 6 M KOH as an electrolyte, respectively. For comparison, a Pt/C+RuO_2 catalyst (mass ratio: 1:1) and a Fe_1/NC catalyst were used as controls. The device configuration is depicted in **Figure 4**a. The Fe SAs/NC-based battery (Figure 4b) exhibits a high open-circuit voltage (OCV) of 1.46 V, larger than that of the Pt/C+RuO_2 (1.41 V) and Fe_1/NC (1.39 V). Charging/discharging polarization curves of catalysts were recorded and a smaller voltage gap was observed for Fe SAs/NC, implying an excellent rechargeability (Figure 4c). In Figure 4d, Fe SAs/NC-based battery shows a maximum peak power density of 306.1 mW cm^{-2}, significantly higher than those of Fe_1/NC (229.9 mW cm^{-2}) and Pt/C+RuO_2 (96.3 mW cm^{-2}) based batteries. Importantly, the Fe SAs/NC-based battery delivered exceptional performance and outperformed most reported results (Table S9, Supporting Information). For example, Zhao et al. fabricated a Fe/Ni hetero-single-atom electrocatalyst and it demonstrated a power density of 148 mW cm^{-2} when used in zinc–air batteries.[49] Wu et al. reported a Cu ISAS/NC electrocatalyst-based zinc–air battery with a high power density of 280 mW cm^{-2}.[50] Du and co-workers synthesized a hierarchically porous Fe—N—C electrocatalyst with a power density of merely 160 mW cm^{-2} in a zinc–air battery.[51] The discharge curves of batteries are shown in Figure 4e,f, and the results demonstrate Fe SAs/NC-based battery can deliver stable discharge potentials at different currents, revealing excellent ORR stability and reversibility. In Figure 4g, the specific capacity of Fe SAs/NC-based battery at different discharge currents of 5 mA cm^{-2}, 10 mA cm^{-2}, and 20 mA cm^{-2} were determined to be 785.4 mAh g^{-1}, 746.9 mAh g^{-1}, and 720.0 mAh g^{-1}, respectively, and the corresponding Zn utilization ratios were calculated to be 95.7%, 91.1%, and 87.8%. In sharp contrast, the Pt/C+RuO_2-based battery at a discharge current of 10 mA cm^{-2} exhibits a low specific capacity of 684.0 mAh g^{-1} with a Zn utilization of merely 83.4%. As shown in Figure 4h, two Fe SAs/NC-based batteries were connected in series and they can light up a blue light-emitting diode (LED) indicator, suggesting excellent operational practicability. The cyclability of zinc–air battery was evaluated under continuous galvanostatic discharge/charge at a current density of 10 mA cm^{-2} with a duration of 30 min per cycle (Figure 4i). Compared with Pt/C+RuO_2-based battery, Fe SAs/NC demonstrated negligible voltage decay within 315 h (630 discharge/charge cycles), revealing superior long-term durability. In addition, a high and robust round-trip efficiency (initial: 65.1%; intermediate: 65.1%; final: 64.7%) was evidenced. More importantly, the zinc–air battery assembled with Fe SAs/NC exhibited superior performance than other benchmarking counterparts in terms of peak power density, specific capacity, and cycling stability.[31,32,40] The highly exposed active sites and unique electronic structure in SACs obtained by different synthesis methods contribute to the excellent bifunctional ORR and OER

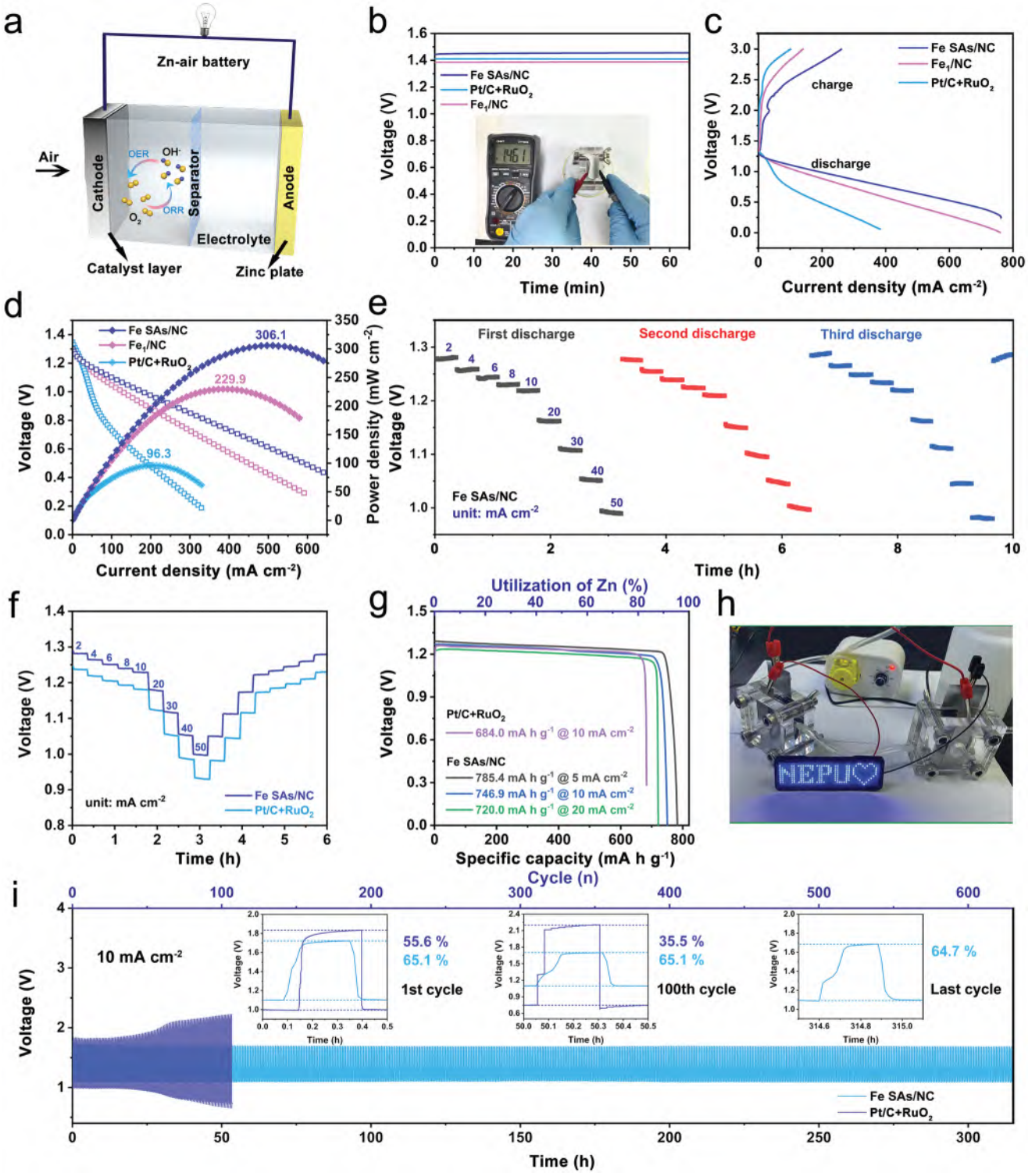

Figure 4. Zinc–air battery performance. a) Schematic diagram of a homemade zinc–air battery. b) Open-circuit plots (inset: OCV recorded by a multimeter). c) Charging/discharging polarization curves. d) Discharging polarization and power density curves. e,f) Galvanostatic discharge curves of zinc–air batteries at different current densities. g) Specific capacities of zinc–air batteries at different discharge current densities. h) Photograph of a LED powered by two zinc–air batteries. i) Galvanostatic discharge/charge cycling curves.

performance in rechargeable zinc–air batteries. Taken together, these results strongly support the superiority of Fe SAs/NC as a potential material in the zinc–air battery.

The ORR activity of catalysts was further evaluated under acidic conditions (0.5 M H_2SO_4). As shown in **Figure 5**a, Fe SAs/NC delivered an ultrahigh activity with an E_{onset} of 0.95 V and

an $E_{1/2}$ of 0.83 V, exceeding the benchmarking Pt/C (0.88 V and 0.74 V) and other references. Importantly, the ORR activity of Fe SAs/NC surpassed most of the reported non-precious candidates in acidic electrolytes (Table S10, Supporting Information). Moreover, the ORR performance of Fe SAs/NC also exceeded those of metal–organic framework (MOF)-derived non-precious metal based single-atom catalysts with similar or even higher metal loadings in alkaline and acidic conditions.[13,32,33,52,53] Compared with these references (Figure 5b), a smaller Tafel slope obtained for Fe SAs/NC (66.2 mV dec^{-1}) highlights its outstanding ORR kinetics. The J_k of catalysts at 0.60 and 0.70 V were calculated, with Fe SAs/NC achieving the highest J_k of 100.00 mA cm^{-2} and 45.45 mA cm^{-2}, respectively. These values are superior to those of Fe_1/NC, Pt/C, NC, and NC (ZIF-8). The calculated C_{dl} of Fe SAs/NC presents a higher value of 4.20 mF cm^{-2} (Figure S39, Supporting Information), implying the largest electrochemical active area and high accessibility of active sites. The electron transfer number was determined to be 4.18 for Fe SAs/NC by the K–L equation (Figure 5d). The RRDE results (Figure S40, Supporting Information) further confirm the desired Pt-like 4-electron ORR pathway with high H_2O selectivity. In sharp contrast, the reference catalysts show inferior selectivity toward the 4-electron ORR pathway. Following addition of KSCN into 0.5 M H_2SO_4, the E_{onset} and $E_{1/2}$ of Fe SAs/NC showed serious activity decay (Figure 5f). After rinsing with water, the ORR activity of Fe SAs/NC was recovered in 0.1 M KOH; this results from the detachment of SCN^- on Fe sites under alkaline conditions (Figure S41, Supporting Information). Moreover, Fe SAs/NC demonstrates a superior tolerance to methanol crossover (Figure 5g); by contrast, the Pt/C

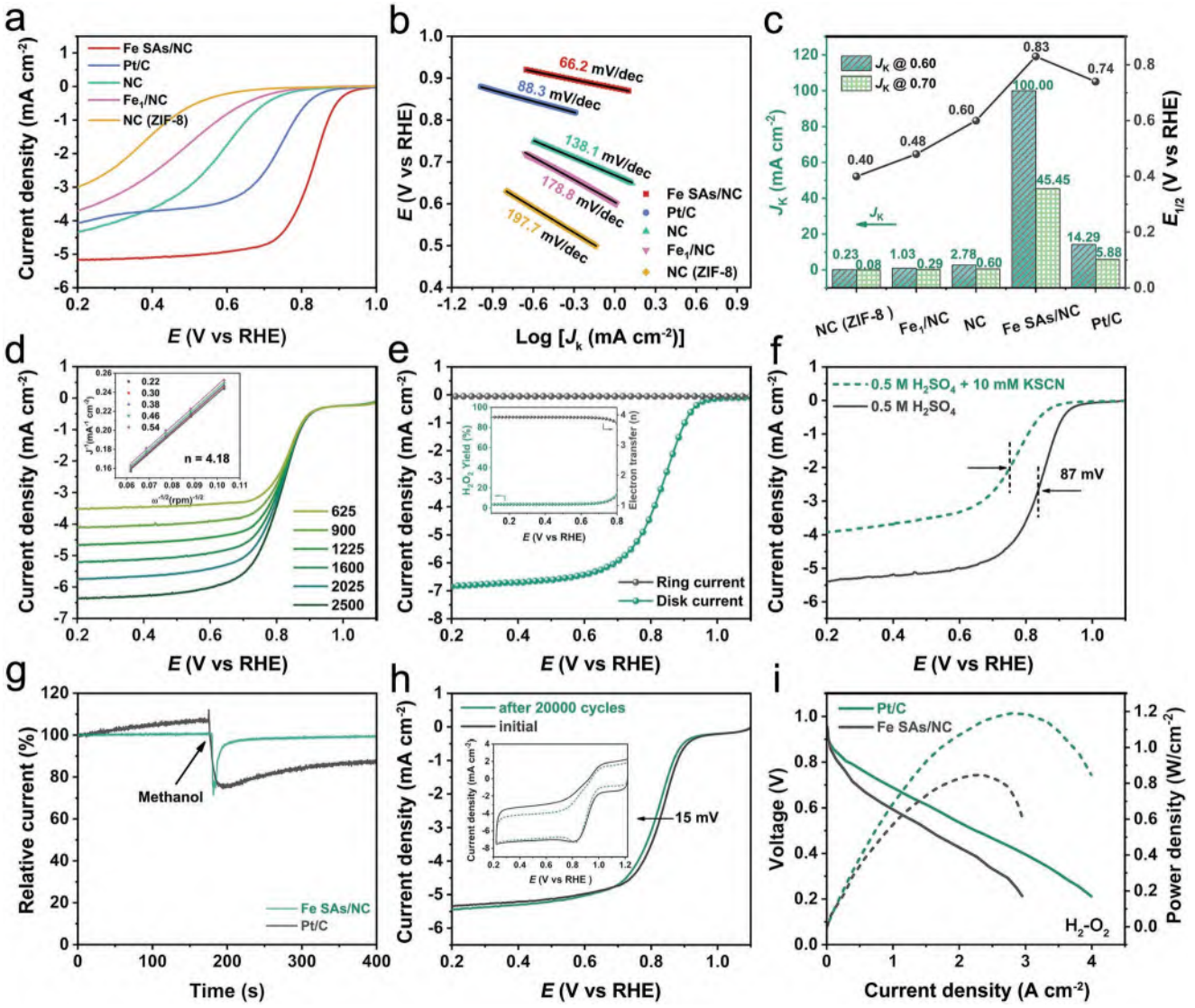

Figure 5. ORR activity of Fe SAs/NC in 0.5 M H_2SO_4 solution. a) ORR polarization curves and b) the corresponding Tafel plots. c) Comparison of J_k at 0.60 V and 0.70 V of samples. d) ORR polarization curves of Fe SAs/NC at different rotating speeds (inset: K–L plots and electron-transfer numbers). e) RRDE measurements (inset: electron transfer number (n) and H_2O_2 selectivity). f) KSCN poisoning results. g) Methanol tolerance results. h) ORR polarization curves of Fe SAs/NC before and after 20 000 potential cycles (inset: the corresponding CV curves). i) PEMFC polarization and power density curves of the H_2–O_2 fuel cell.

catalyst shows a serious activity decay due to the methanol oxidation. Fe SAs/NC catalyst also demonstrates excellent stability with current retention of ≈ 91% after 10 h chronoamperometry measurements (Figure S42, Supporting Information), superior to that of the commercial Pt/C catalyst (≈76%). Importantly, no significant activity decay in $E_{1/2}$ (≈15 mV) is observed for Fe SAs/NC after 20 000 repeated cycles by the accelerated durability and cyclic voltammetry tests (Figure 5h), which is superior to that of Pt/C with ≈51 mV activity loss (Figure S43, Supporting Information). To validate the potential of Fe SAs/NC in practical applications, we assembled the catalyst into a membrane electrode assembly (MEA) in proton exchange membrane fuel cells (PEMFCs). Figure 5i shows the polarization and power density curves of Fe SAs/NC and Pt/C-based MEA in PEMFCs. Fe SAs/NC displayed current densities of 0.95 A cm^2 and 2.86 A cm^2 at 0.60 V and 0.25 V, respectively. Moreover, it demonstrates an impressive peak power density of 850 mW cm^{-2}, which is among the best non-precious-metal catalysts (Table S11, Supporting Information). Compared with Pt/C-based MEA (1190 mW cm^{-2}), the relatively lower peak power density of Fe SAs/NC can be explained by the lower number of active sites in the catalyst.[54–56] The above results demonstrate the promising role of Fe SAs/NC as cathode catalysts in direct methanol fuel cells.

The electrocatalytic ORR activity of Fe SAs/NC was further explored in neutral conditions (0.1 M PBS). Impressively, Fe SAs/NC afforded the best ORR activity with E_{onset} of 0.93 V and $E_{1/2}$ of 0.75 V, exceeding Pt/C (0.92 V and 0.67 V) and other references (Figure S44a and Table S12, Supporting Information). Importantly, its ORR activity was superior to most of the reported Fe catalysts in 0.1 M PBS (Table S12, Supporting Information). Additionally, a smaller Tafel slope of 67.4 mV dec^{-1} was achieved than those of other references (Figure S44b), underscoring the high intrinsic activity. RDE and RRDE results (Figures S45 and S46, Supporting Information) demonstrate the 4-electron ORR pathway of Fe SAs/NC over the potential range from 0.2 V to 0.8 V. Moreover, Fe SAs/NC possesses the largest electrochemical active surface area (Figure S47, Supporting Information), highlighting its favorable role in efficiently catalyzing the ORR in neutral conditions.

To explore the origin of the exceptional bifunctional catalytic activity of Fe SAs/NC, density functional theory (DFT) calculations were performed. 9 types of models were constructed for $Fe_1N_4O_1$ and type i was found to have the lowest formation energy, suggesting that this structure is energetically more favorable than others (Figure S48, Supporting Information). Bader charge analysis and differential charge density distributions are shown in **Figure 6**a,b. Due to the unique $Fe_1N_4O_1$ configuration, more charges are transferred from the Fe center to the nearby N and O elements in comparison to that of the Fe_1N_4 structure. This reveals that the induction of O can induce charge spatial redistribution around the Fe_1N_4 center and optimize the adsorption/desorption behavior of adsorbed oxygenated intermediates, thus affecting the catalytic properties. Based on the projected density of states (PDOS) and d-band theory, a downshift of the d-band center of –0.90 eV for $Fe_1N_4O_1$ indicates a lowered energy level and elevated occupancy of the antibonding states (Figure 6c–e).[57,58] Moreover, the change in electronic states facilitates tuning the metal-adsorbate interaction which was too strong in Fe_1N_4.[43,59] To confirm the downshift in the d-band center in $Fe_1N_4O_1$ correlates with a weakened binding with molecular oxygen, Bader charge and differential charge density were conducted (Figures S49 and S50, Supporting Information). The results reveal that a significantly lower amount of charge is transferred from Fe to the adsorbed O_2 for $Fe_1N_4O_1$. This result in weakened adsorption between O_2 and $Fe_1N_4O_1$. From the viewpoint of thermodynamics, the weakened adsorption should be beneficial to ORR because of the alleviated strong binding of ORR intermediates on the Fe center.[43,60] The weakened binding was further verified by the PDOS and adsorption energy results shown in Figures S51 and S52 (Supporting Information).

The calculated free energy diagrams of the ORR on $Fe_1N_4O_1$ and Fe_1N_4 at pH = 13 are shown in Figure 6f,g and Table S13 (Supporting Information). The details of the optimized geometry of $Fe_1N_4O_1$ and Fe_1N_4 with adsorbed intermediates (O_2*, OOH*, O*, and OH*) are presented in Figures S53 and S54 (Supporting Information). Compared with Fe_1N_4, the free energies at zero electrode potential (U = 0 V vs RHE) in $Fe_1N_4O_1$ demonstrate a downhill and thermodynamically spontaneous exothermic process. In contrast, the first elementary step (the reduction of O_2 to OOH*) from Fe_1N_4 has the highest endothermic energy of 0.28 eV. The theoretical limiting potentials of $Fe_1N_4O_1$ and Fe_1N_4 are calculated to be 0.19 V and –0.28 V, respectively. The higher theoretical limiting potential suggests that the $Fe_1N_4O_1$ is more active to catalyze ORR under alkaline conditions. Under the equilibrium potential (U = 0.46 V), the first elementary step (the reduction of O_2 to OOH*) for $Fe_1N_4O_1$ and Fe_1N_4 is the limiting step. The corresponding free energy change of $Fe_1N_4O_1$ (0.28 eV) is much smaller than that of Fe_1N_4 (0.75 eV), manifesting that the $Fe_1N_4O_1$ site is thermodynamically favorable.

Then, the OER mechanisms of $Fe_1N_4O_1$ and Fe_1N_4 at pH = 13 were investigated and the corresponding free energy profiles are shown in Figure 6h,i and Table S14 (Supporting Information). At U = 0 V, the free energy difference of $Fe_1N_4O_1$ in the limiting step (deprotonation of OH*) is 1.05 eV, which is smaller than that of 1.16 eV for Fe_1N_4 (oxidation of O* to OOH*). At U = 0.46 V (equilibrium potential), the corresponding limiting step values are 0.59 eV and 0.70 eV for $Fe_1N_4O_1$ and Fe_1N_4, respectively. These results indicate that the induction of O in $Fe_1N_4O_1$ can effectively reduce the energy barrier to strongly accelerate the OER kinetics. Taken together, facilitating the formation of OOH* for the ORR and accelerating deprotonation of OH* for OER are the keys for Fe SAs/NC to serve as an efficient bifunctional catalyst.

Finally, the ORR mechanisms of $Fe_1N_4O_1$ and Fe_1N_4 at pH = 0 were investigated. The corresponding free energy diagrams are shown in Figure 6j,k and Table S15 (Supporting Information). Each ORR step for the two models is thermodynamically downslope at U = 0 V, implying all these elementary steps are exothermic. The theoretical limiting potential of $Fe_1N_4O_1$ is up to 0.96 V, significantly larger than that of Fe_1N_4 (0.48 V), implying $Fe_1N_4O_1$ has a better catalytic activity toward ORR under acidic conditions. At U = 1.23 V (equilibrium potential), several endothermic steps are observed in the two models. The highest endothermic energy of 0.27 eV was found for $Fe_1N_4O_1$ which suggests the first step is the limiting step. By contrast, a significantly higher endothermic energy of

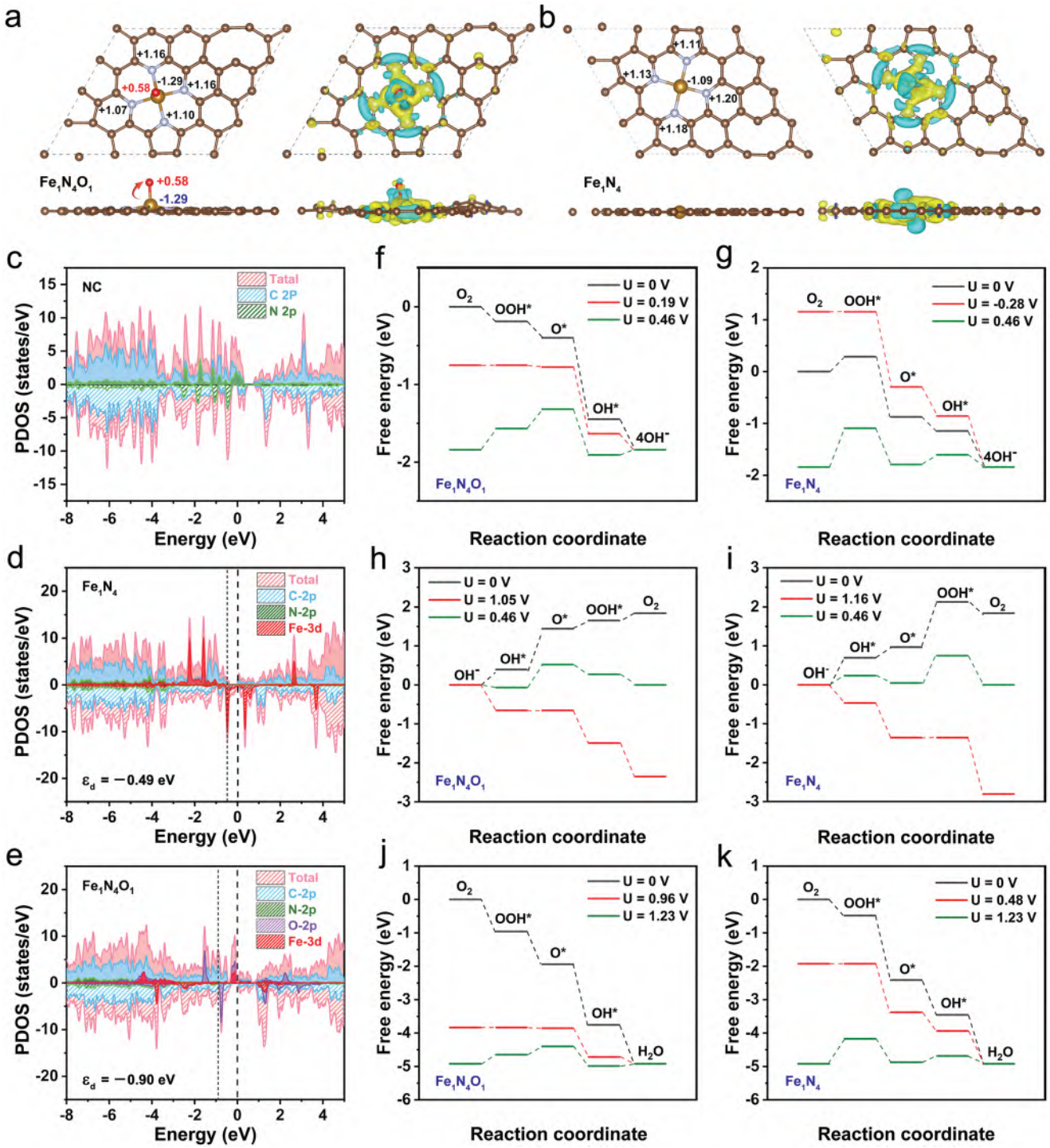

Figure 6. Density functional theory calculations. a,b) Bader charge and differential charge density of $Fe_1N_4O_1$ (a) and Fe_1N_4 (b) (isosurface is 0.003 e Å^{-3}). The charge accumulation and depletion are colored in yellow and cyan. c–e) Projected density of states of NC (c), Fe_1N_4 (d), and $Fe_1N_4O_1$ (e). f,g) Calculated free energy diagrams of the ORR on $Fe_1N_4O_1$ (f) and Fe_1N_4 (g) at pH = 13. h,i) Calculated free energy diagrams of the OER on $Fe_1N_4O_1$ (h) and Fe_1N_4 (i) at pH = 13. j,k) Calculated free energy diagrams of the ORR on $Fe_1N_4O_1$ (j) and Fe_1N_4 (k) at pH = 0.

0.75 eV was observed for Fe_1N_4 (the first step). These results demonstrate that $Fe_1N_4O_1$ possesses a lower activation energy barrier in comparison to Fe_1N_4 (more sluggish kinetics). Taken together, these findings demonstrate Fe SAs/NC possesses exceptional ORR/OER bifunctional electrocatalytic activity.

3. Conclusion

We have demonstrated a single Fe atom electrocatalyst supported over mesoporous NC material with an engineered coordination environment and electronic structure that confers

outstanding ORR and OER performance. This Fe SAs/NC possesses a higher specific surface area and mesoporosity, favoring efficient mass transport and high utilization of metal sites. Due to the optimized electronic metal–support interactions, the Fe SAs/NC demonstrated excellent ORR activity, durability, and tolerance to methanol, superior to the benchmarking Pt/C catalyst at all pH values. Moreover, it delivered impressive OER activity under alkaline conditions. Importantly, the Fe SAs/NC-based zinc–air battery exhibited a high peak power density of 306.1 mW cm^{-2}, a large specific capacity of 746.9 mAh g^{-1}, and robust cycling stability beyond 315 h, exceeding those of the previously reported non-precious-metal catalysts and the benchmarking Pt/C+RuO_2 catalysts. Theoretical calculations highlight the merit of electronic structure engineering can effectively induce charge redistribution around the metal center and optimize the binding of oxygenated intermediates, thereby ultimately tuning catalytic properties. This work shed light on the rational design of single-atom catalysts by electronic structure engineering for efficient electrocatalysis.

Supporting Information

Supporting Information is available from the Wiley Online Library or from the author.

Acknowledgements

S.J. and C.X. contributed equally to this work. This work was supported by the Outstanding Youth Project of the Natural Science Foundation of Heilongjiang Province (YQ2022B002), the Scientific Research Foundation for Returned Scholars of Heilongjiang Province of China (719900091), and the Heilongjiang Touyan Innovation Team Program.

Conflict of Interest

The authors declare no conflict of interest.

Data Availability Statement

The data that support the findings of this study are available from the corresponding author upon reasonable request.

Keywords

iron, oxygen evolution reaction, oxygen reduction reaction, single atom catalysis, zinc–air batteries

Received: October 19, 2022
Revised: November 24, 2022
Published online: December 29, 2022

[1] J. G. Chen, R. M. Crooks, L. C. Seefeldt, K. L. Bren, R. M. Bullock, M. Y. Darensbourg, P. L. Holland, B. Hoffman, M. J. Janik, A. K. Jones, M. G. Kanatzidis, P. King, K. M. Lancaster, S. V. Lymar, P. Pfromm, W. F. Schneider, R. R. Schrock, *Science* **2018**, *360*, 837.
[2] M. K. Debe, *Nature* **2012**, *486*, 43.
[3] Z. W. She, J. Kibsgaard, C. F. Dickens, I. Chorkendorff, J. K. Nørskov, T. F. Jaramillo, *Science* **2017**, *355*, 146.
[4] A. Kulkarni, S. Siahrostami, A. Patel, J. K. Nørskov, *Chem. Rev.* **2018**, *118*, 2302.
[5] G. Wu, K. L. More, C. M. Johnston, P. Zelenay, *Science* **2011**, *332*, 443.
[6] H. Mistry, A. S. Varela, S. Kühl, P. Strasser, B. R. Cuenya, *Nat. Rev. Mater.* **2016**, *1*, 16009.
[7] S. Ding, J. A. Barr, Q. Shi, Y. Zeng, P. Tieu, Z. Lyu, L. Fang, T. Li, X. Pan, S. P. Beckman, D. Du, H. Lin, J. C. Li, G. Wu, Y. Lin, *ACS Nano* **2022**, *16*, 15165.
[8] Y. Zhao, X. F. Lu, G. Fan, D. Luan, X. Gu, X. D. Lou, *Angew. Chem., Int. Ed.* **2022**, *61*, 202212542.
[9] H. Shen, H. Peng, R. Cao, L. Yang, Y. Gao, A. Turak, T. Thomas, X. Guo, Y. Zhu, J. Wang, M. Yang, *J. Phys. Chem. Lett.* **2021**, *12*, 517.
[10] X. Hu, S. Chen, L. Chen, Y. Tian, S. Yao, Z. Lu, X. Zhang, Z. Zhou, *J. Am. Chem. Soc.* **2022**, *144*, 18144.
[11] G.-L. Chai, K. Qiu, M. Qiao, M.-M. Titirici, C. Shang, Z. Guo, *Energy Environ. Sci.* **2017**, *10*, 1186.
[12] J. Sheng, S. Sun, G. Jia, S. Zhu, Y. Li, *ACS Nano* **2022**, *16*, 15994.
[13] K. Wang, Z. Lu, J. Lei, Z. Liu, Y. Li, Y. Cao, *ACS Nano* **2022**, *16*, 11944.
[14] H. T. Chung, D. A. Cullen, D. Higgins, B. T. Sneed, E. F. Holby, K. L. More, P. Zelenay, *Science* **2017**, *357*, 479.
[15] A. A. Gewirth, J. A. Varnell, A. M. DiAscro, *Chem. Rev.* **2018**, *118*, 2313.
[16] B. Zhang, X. Zheng, O. Voznyy, R. Comin, M. Bajdich, M. García-Melchor, L. Han, J. Xu, M. Liu, L. Zheng, F. P. G. d. Arquer, C. T. Dinh, F. Fan, M. Yuan, E. Yassitepe, N. Chen, T. Regier, P. Liu, Y. Li, P. D. Luna, A. Janmohamed, H. L. Xin, H. Yang, A. Vojvodic, E. H. Sargent, *Science* **2016**, *352*, 333.
[17] J. Hulva, M. Meier, R. Bliem, Z. Jakub, F. Kraushofer, M. Schmid, U. Diebold, C. Franchini, G. S. Parkinson, *Science* **2021**, *371*, 375.
[18] C. Gao, J. Low, R. Long, T. Kong, J. Zhu, Y. Xiong, *Chem. Rev.* **2020**, *120*, 12175.
[19] Z. Li, D. Wang, Y. Wu, Y. Li, *Natl. Sci. Rev.* **2018**, *5*, 673.
[20] X. Liang, N. Fu, S. Yao, Z. Li, Y. Li, *J. Am. Chem. Soc.* **2022**, *144*, 18155.
[21] S. Ji, X. Lu, M. Zhang, L. Leng, H. Liu, K. Yin, C. Xu, C. He, J. H. Horton, J. Zhan, Z. Li, *Chem. Eng. J.* **2023**, *452*, 139205.
[22] Z. Li, Y. Chen, X. Lu, H. Li, L. Leng, T. Zhang, J. H. Horton, *Nano Res.* **2022**, *15*, 4023.
[23] Z. Li, L. Leng, X. Lu, M. Zhang, Q. Xu, J. H. Horton, J. Zhu, *Nano Res.* **2021**, *15*, 3114.
[24] Z. Li, H. Li, Z. Yang, X. Lu, S. Ji, M. Zhang, J. H. Horton, H. Ding, Q. Xu, J. Zhu, J. Yu, *Small* **2022**, *18*, 2201092.
[25] Z. Li, M. Zhang, X. Dong, S. Ji, L. Zhang, L. Leng, H. Li, J. H. Horton, Q. Xu, J. Zhu, *Appl. Catal. B* **2022**, *313*, 121462.
[26] X. Dong, Y. Jia, M. Zhang, S. Ji, L. Leng, J. H. Horton, C. Xu, C. He, Q. Tan, J. Zhang, Z. Li, *Chem. Eng. J.* **2023**, *451*, 138660.
[27] X. Wan, J. Shui, *ACS Energy Lett.* **2022**, *7*, 1696.
[28] Y. S. Wei, M. Zhang, R. Zou, Q. Xu, *Chem. Rev.* **2020**, *120*, 12089.
[29] Z. Zhuang, Y. Li, R. Yu, L. Xia, J. Yang, Z. Lang, J. Zhu, J. Huang, J. Wang, Y. Wang, L. Fan, J. Wu, Y. Zhao, D. Wang, Y. Li, *Nat. Catal.* **2022**, *5*, 300.
[30] G. Giannakakis, M. Flytzani-Stephanopoulos, E. C. H. Sykes, *Acc. Chem. Res.* **2019**, *52*, 237.
[31] Y. Pan, S. Liu, K. Sun, X. Chen, B. Wang, K. Wu, X. Cao, W. C. Cheong, R. Shen, A. Han, Z. Chen, L. Zheng, J. Luo, Y. Lin, Y. Liu, D. Wang, Q. Peng, Q. Zhang, C. Chen, Y. Li, *Angew. Chem., Int. Ed.* **2018**, *57*, 8614.
[32] J. Han, X. Meng, L. Lu, J. Bian, Z. Li, C. Sun, *Adv. Funct. Mater.* **2019**, *29*, 1808872.
[33] C.-X. Zhao, J.-N. Liu, J. Wang, C. Wang, X. Guo, X.-Y. Li, X. Chen, L. Song, B.-Q. Li, Q. Zhang, *Sci. Adv.* **2022**, *8*, eabn5091.

[34] C. Vogt, B. M. Weckhuysen, *Nat. Rev. Chem.* **2022**, *6*, 89.
[35] M. Xiao, J. Zhu, S. Li, G. Li, W. Liu, Y.-P. Deng, Z. Bai, L. Ma, M. Feng, T. Wu, D. Su, J. Lu, A. Yu, Z. Chen, *ACS Catal.* **2021**, *11*, 8837.
[36] S. Chen, T. Luo, X. Li, K. Chen, J. Fu, K. Liu, C. Cai, Q. Wang, H. Li, Y. Chen, C. Ma, L. Zhu, Y. R. Lu, T. S. Chan, M. Zhu, E. Cortes, M. Liu, *J. Am. Chem. Soc.* **2022**, *144*, 14505.
[37] X. Wan, X. Liu, Y. Li, R. Yu, L. Zheng, W. Yan, H. Wang, M. Xu, J. Shui, *Nat. Catal.* **2019**, *2*, 259.
[38] F. Zaera, *Chem. Rev.* **2022**, *122*, 8594.
[39] Y. Chen, R. Rana, T. Sours, F. D. Vila, S. Cao, T. Blum, J. Hong, A. S. Hoffman, C. Y. Fang, Z. Huang, C. Shang, C. Wang, J. Zeng, M. Chi, C. X. Kronawitter, S. R. Bare, B. C. Gates, A. R. Kulkarni, *J. Am. Chem. Soc.* **2021**, *143*, 20144.
[40] S. Ji, T. Liu, L. Leng, H. Liu, J. Zhang, M. Zhang, Q. Xu, J. Zhu, M. Qiao, Y. Wang, J. H. Horton, Z. Li, *Appl Catal B* **2023**, *320*, 121987.
[41] Z. Li, L. Leng, S. Ji, M. Zhang, H. Liu, J. Gao, J. Zhang, J. H. Horton, Q. Xu, J. Zhu, *J Energy Chem* **2022**, *73*, 469.
[42] L. Liu, A. Corma, *Chem. Rev.* **2018**, *118*, 4981.
[43] F. Liu, L. Shi, X. Lin, D. Yu, C. Zhang, R. Xu, D. Liu, J. Qiu, L. Dai, *Appl. Catal. B* **2022**, *302*, 120860.
[44] G. Chen, P. Liu, Z. Liao, F. Sun, Y. He, H. Zhong, T. Zhang, E. Zschech, M. Chen, G. Wu, J. Zhang, X. Feng, *Adv. Mater.* **2020**, *32*, 1907399.
[45] Y. Chen, Z. Li, Y. Zhu, D. Sun, X. Liu, L. Xu, Y. Tang, *Adv. Mater.* **2019**, *31*, 1806312.
[46] Z. Yang, Y. Wang, M. Zhu, Z. Li, W. Chen, W. Wei, T. Yuan, Y. Qu, Q. Xu, C. Zhao, X. Wang, P. Li, Y. Li, Y. Wu, Y. Li, *ACS Catal.* **2019**, *9*, 2158.
[47] P. Peng, L. Shi, F. Huo, C. Mi, X. Wu, S. Zhang, Z. Xiang, *Sci. Adv.* **2019**, *5*, 2322.
[48] H. B. Yang, J. Miao, S. Hung, J. Chen, H. B. Tao, X. Wang, L. Zhang, R. Chen, J. Gao, H. M. Chen, L. Dai, B. Liu, *Sci. Adv.* **2016**, *2*, 1501122.
[49] Z. Zhu, H. Yin, Y. Wang, C. H. Chuang, L. Xing, M. Dong, Y. R. Lu, G. Casillas-Garcia, Y. Zheng, S. Chen, Y. Dou, P. Liu, Q. Cheng, H. Zhao, *Adv. Mater.* **2020**, *32*, 2004670.
[50] Z. Yang, B. Chen, W. Chen, Y. Qu, F. Zhou, C. Zhao, Q. Xu, Q. Zhang, X. Duan, Y. Wu, *Nat. Commun.* **2019**, *10*, 3734.
[51] H. Xu, D. Wang, P. Yang, L. Du, X. Lu, R. Li, L. Liu, J. Zhang, M. An, *Appl. Catal. B* **2022**, *305*, 121040.
[52] Q. Liu, X. Liu, L. Zheng, J. Shui, *Angew. Chem., Int. Ed.* **2018**, *57*, 1204.
[53] X. Wang, H. Zhu, C. Yang, J. Lu, L. Zheng, H.-P. Liang, *Carbon* **2022**, *191*, 393.
[54] M. Xiao, J. Zhu, G. Li, N. Li, S. Li, Z. P. Cano, L. Ma, P. Cui, P. Xu, G. Jiang, H. Jin, S. Wang, T. Wu, J. Lu, A. Yu, D. Su, Z. Chen, *Angew. Chem., Int. Ed.* **2019**, *58*, 9640.
[55] Y. Chen, S. Ji, S. Zhao, W. Chen, J. Dong, W. C. Cheong, R. Shen, X. Wen, L. Zheng, A. I. Rykov, S. Cai, H. Tang, Z. Zhuang, C. Chen, Q. Peng, D. Wang, Y. Li, *Nat. Commun.* **2018**, *9*, 5422.
[56] R. Gao, J. Wang, Z.-F. Huang, R. Zhang, W. Wang, L. Pan, J. Zhang, W. Zhu, X. Zhang, C. Shi, J. Lim, J.-J. Zou, *Nat. Energy* **2021**, *6*, 614.
[57] X. Zhang, X. Xu, S. Yao, C. Hao, C. Pan, X. Xiang, Z. Q. Tian, P. K. Shen, Z. Shao, S. P. Jiang, *Small* **2022**, *18*, 2105329.
[58] Q. Hu, K. Gao, X. Wang, H. Zheng, J. Cao, L. Mi, Q. Huo, H. Yang, J. Liu, C. He, *Nat. Commun.* **2022**, *13*, 3958.
[59] L. Yu, Y. Li, Y. Ruan, *Angew. Chem., Int. Ed.* **2021**, *60*, 25296.
[60] G. Yang, J. Zhu, P. Yuan, Y. Hu, G. Qu, B. A. Lu, X. Xue, H. Yin, W. Cheng, J. Cheng, W. Xu, J. Li, J. Hu, S. Mu, J. N. Zhang, *Nat. Commun.* **2021**, *12*, 1734.